Probabilistic examination of the change in eigenfrequencies of an offshore wind turbine under progressive scour incorporating soil spatial variability

Prendergast, L. J.; Reale, C.; Gavin, K.

DOI
10.1016/j.marstruc.2017.09.009

Publication date
2018

Document Version
Accepted author manuscript

Published in
Marine Structures

Published in *Marine Structures* 57 **2018** pp.87-104

Probabilistic examination of the change in eigenfrequencies of an offshore wind turbine under progressive scour incorporating soil spatial variability

Prendergast, L.J.[a,1], Reale. C.[a,2], Gavin, K.[a,3]

[a] Faculty of Civil Engineering and Geosciences,
Delft University of Technology,
Building 23,
Stevinweg 1 / PO-box 5048,
2628 CN Delft / 2600 GA Delft,
The Netherlands

[2]Corresponding author

Email: [1]l.j.prendergast@tudelft.nl, [2]c.reale@tudelft.nl, [3]k.g.gavin@tudelft.nl

Abstract

The trend for development in the offshore wind sector is towards larger turbines in deeper water. This results in higher wind and wave loads on these dynamically sensitive structures. Monopiles are the preferred foundation solution for offshore wind structures and have a typical expected design life of 20 years. These foundations have strict serviceability tolerances (e.g. mudline rotation of less than 0.25° during operation). Accurate determination of the system frequency is critical in order to ensure satisfactory performance over the design life, yet determination of the system stiffness and in particular the operational soil stiffness remains a significant challenge. Offshore site investigations typically focus on the determination of the soil conditions using Cone Penetration Test (CPT) data. This test gives large volumes of high quality data on the soil conditions at the test location, which can be correlated to soil strength and stiffness parameters and used directly in pile capacity models. However, a combination of factors including; parameter transformation, natural variability, the relatively small volume of the overall sea bed tested and operational effects such as the potential for scour development during turbine operation lead to large uncertainties in the soil stiffness values used in design. In this paper, the effects of scour erosion around unprotected foundations on the design system frequencies of an offshore wind turbine is investigated numerically. To account for the uncertainty in soil-structure interaction stiffness for a given offshore site, a stochastic ground model is developed using the data resulting from CPTs as inputs. Results indicate that the greater the depth of scour, the less certain a frequency-based SHM technique would be in accurately assessing scour magnitude based solely on first natural frequency measurements. However, using Receiver Operating Characteristic (ROC) curve analysis, the chance of detecting the *presence* of scour from the output frequencies is improved significantly and even modest scour depths of 0.25 pile diameters can be detected.

Keywords: Scour; Offshore Wind; Uncertainty; Frequency; SHM; Spatial Variability

1.0 Introduction

In order to meet increasing energy demands, reduce reliance on non-renewable sources and increase energy security, alternative and renewable energies are in high demand. In Europe, offshore wind turbines provided over 11,000 MW of grid-connected capacity at the end of 2015 [1], supplying 1.5% of the electricity consumption demand of the European Union (EU) [2]. The offshore wind industry is continually undergoing rapid development, tending towards larger capacity turbines, ever-increasing hub heights and locations further offshore in deeper waters. This rapid development is a challenge for foundation design, and design methods are constantly evolving [3,4].

To date, over 80% of offshore turbines are founded on monopiles, followed by 9% founded on Gravity Base Foundations (GBFs) and approximately 5% on jacket structures [1]. Other solutions include Tripods, Tripiles, floating solutions as well as experimental foundation concepts. Monopiles are by far the preferred foundation solution with typical diameters (D) ranging from 4-6m and larger with typical penetrations (L) of 20-30m [5,6]. As turbines grow larger and water depths increase monopiles with diameters of up to 10m are being planned, leading to increased foundation costs. Foundations typically account for 30% of the cost of the entire system [7]. Larger monopiles will lead to increased lateral hydrodynamic loads, impacting the monopile in the horizontal direction, resulting in significant shear forces and overturning moments. Foundations typically resists this loading through flexural action and rigid rotation and the ultimate capacity is governed by soil strength properties or the structural properties of the pile. Rigid monopiles with slenderness ratios, length normalised by diameter (L/D), of 5 and below have more uncertain lateral load-resistance characteristics as the design methods for offshore piles were originally developed for long, slender piles [8–11] which flex under an applied lateral load.

Scour erosion around monopiles reduces the lateral load bearing capacity as well as the soil-structure interface stiffness [12] and can result in significant changes to load effects at the mudline level. Scour occurs when the near bed shear stresses applied by hydraulic action exceed the threshold shear stress at which sediment commences movement and occurs as a result of the obstruction caused by the monopile changing the waterflow characteristics locally [13]. It is a complicated mechanism and is environment dependent. In rivers, scour generally occurs under steady current conditions whereas in the marine environment, it occurs due to current, tides and waves [14]. The combined action of current and waves typically gives rise to lower ultimate scour depths than under current only conditions [10,15], however the interaction is complex and uncertain.

Scour alters the dynamic characteristics of structures, a phenomena that has led to significant research interest related to the performance of river bridges [16–23]. From this research there is consensus that scour reduces the foundation stiffness for bridges. In the offshore environment however, there is uncertainty about the effects of scour on the strength and stiffness properties of soil and the combined effects of load cycling and pore pressure accumulation [6]. In marine conditions, combined effects from currents and waves lead to variations in the equilibrium scour depth, with erosion and backfilling both occurring. Unlike in rivers under live-bed erosion conditions [24], where the deposited material typically has lower strength and stiffness properties, the wave action can densify this material potentially restoring stiffness to pre-scour levels or higher [25]. The uncertainty associated with the effects of scour on the strain dependant stiffness behaviour of the remaining soil, cyclic load response, bearing capacity and other factors potentially makes scour occurrence a critical safety issue.

The analysis in this paper builds on the study presented by Prendergast et al. [26], which examined the effect of scour on the natural system frequency of an offshore turbine under three idealised soil profiles. The model is expanded in the present work to investigate the effect of spatial variability in soil properties derived from measured Cone Penetration Test (CPT) data on the system frequencies of a typical turbine under scoured conditions. A sample of twenty deep CPT profiles measured in a reclaimed area of Rotterdam Harbour were used to generate 50,000 hypothetical spatially-correlated CPT profiles for the statistical analyses. A Monte-Carlo analysis was performed to derive the likely system frequencies for a typical offshore turbine considering a range of scour depths. The variation in frequency from the spatial uncertainty of the ground conditions and with scour is investigated, with a view to understanding whether the magnitude of the changes could be detected within a SHM framework.

2.0 Test Site

The ground model developed in this paper is based on data from the Port of Rotterdam, Netherlands. The site was originally located offshore in the North sea, but was reclaimed by the Dutch Authorities in the 1970s [27]. The site consists of predominately Holocene era sands to a depth of approximately 25m below existing ground level (egl) with bulk unit weights ranging from 18.5 to 20.5 kN m^{-3}. The relative density (D_r) is approximately 50%. Some modest clay to clayey silt lenses of varying thickness are found in between primarily close to ground level, with a maximum thickness of approximately 1m to 1.5m. The bulk unit weight of the clay layers is in the range of 15 to 18 kN m^{-3}. Some medium coarse Pleistocene sands are found at a depth of 24 to 25 m below egl [27], with a bulk unit weight between 19 and 20 kN m^{-3}, a D_r of 80% and φ' between 35° and 37°. The perched water table elevation ranges from a minimum of 3.5m below egl to a maximum of 1m below egl. Twenty CPT q_c profiles were measured at the site and corrected to the ordnance datum (NAP). The relative locations of these CPT profiles are shown in Fig. 1. Fig. 2 shows the CPT q_c profiles measured, with the average and maximum/minimum envelopes also shown. As is evident, there are two distinct layers present in the profiles, transitioning at approximately 23 – 25 m below ground level.

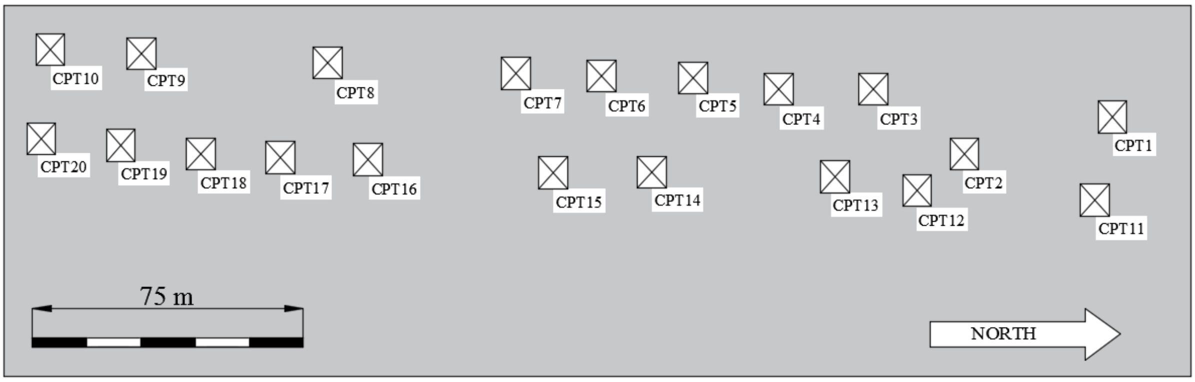

Fig. 1 Cone Penetration Test (CPT) spatial layout at Rotterdam Harbour

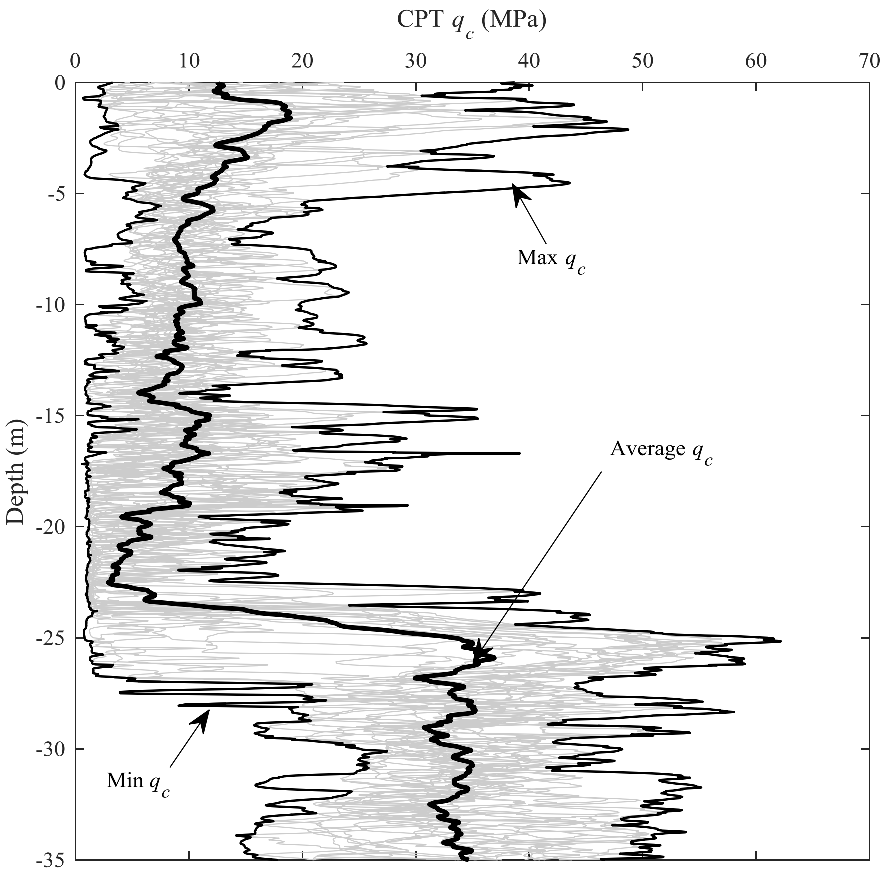

Fig. 2 CPT q_c profiles with maximum and minimum envelopes

3.0 Stochastic ground model

Soil is a naturally heterogeneous material, understanding how it varies is essential to the development of accurate mechanics based ground models, which can encapsulate and subsequently represent soil physical properties. Traditionally variability within soil was accounted for by subdividing the soil into a number of discrete layers, with each layer having a different set of deterministic soil parameters to describe the soil properties within that layer [28,29]. Naturally, given the significant uncertainty present in such an approach, conservative values have to be chosen.

In an effort to eradicate such gross oversimplifications, probabilistic techniques have come to the fore for geotechnical applications [30–34]. Such approaches utilise all of the available data from a soil layer in the form of a probability distribution. While the majority of structural engineering problems can be modelled using a simple random variable approach, the stratified nature and heterogenic composition of soil demands a more complex stochastic approach [35]. To account for this soil is frequently modelled using a number of layered non-homogeneous random fields (2D or 3D) or processes (1D) [36–39]. These random fields or processes model the scope of a given property's variance and define how it varies temporally and/or spatially.

For variables that can be described using normal and log-normal distributions (See Fig. 3(a)) the random process of a soil property can be described in terms of three variables, namely mean, standard deviation and a third term describing the spatial variability, in this case the scale of fluctuation (θ), see Fig. 3(b). The scale of fluctuation is the distance over which soil properties are significantly correlated [40,41]. While the mean and standard deviation are easy to obtain from a given dataset, determining the scale of fluctuation is somewhat more complicated. The general procedure adopted in this paper, to generate spatially correlated CPT tip resistance (q_c) profiles in the vertical direction, is outlined below. As this is a complex field of study in its own right, interested readers are directed to [42,43] for a more in depth discussion and alternative methods for investigating spatial variability. Only a fundamental overview is provided herein for the present application.

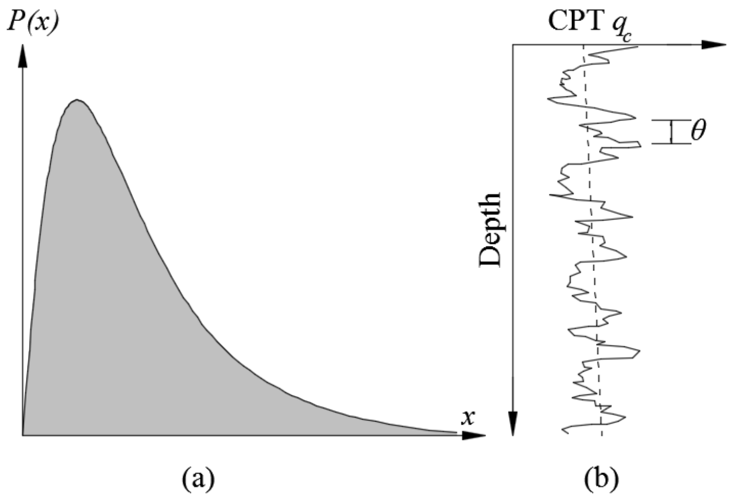

Fig. 3 (a) Initial lognormal distribution defined by mean and standard deviation at a given depth, (b) Scale of fluctuation (θ) adjusts the general shape of distribution to account for spatial variability

To determine the CPT spatial correlation structure in the vertical direction it is necessary to first remove any underlying trend from the data. Typically, only first order trends (for example the strength increase with depth typically seen in normally consolidated soil deposits) are considered as higher order trends may result in overfitting and their use would demand further justification. By redefining the mean and standard deviation such that they are functions of depth (See Fig. 3(b)), the mean trend can be removed from the dataset using a curve fitting approach, thus isolating any variability. This variability can then be fitted to a spatial correlation structure. Following the removal of any discernible trend, the soil property (in this case q_c) for a normal distribution can be described by Eq.(1).

$$q_c = \mu + \sigma \mathbf{G} \quad [1]$$

where μ is the mean value described at a depth *z* using Eq. (2), σ is the standard deviation at the same depth and **G** is a matrix containing *n* spatially correlated normal random processes of zero mean and unit variance which account for the vertical spatial correlation structure.

$$\mu(z) = a_i + b_i z \quad [2]$$

where a_i is the value of the mean trend at the beginning of the *ith* layer, b_i is the slope of that trend at the same layer and *z* is the depth into the stratum.

When the linear depth trend of each q_c profile in the dataset is removed, the standard deviation of the detrended tip resistances is calculated. Normalised detrended tip resistances are then obtained by dividing the individual detrended CPTs by their respective standard deviations. This approach produces normal random processes with a mean of zero and a standard deviation of 1. These normal random processes can be used to estimate the spatial correlation structure $\hat{\rho}(\tau_j)$ of the CPTs with depth, see Eq. (3).

$$\hat{\rho}(\tau_j) = \frac{1}{\sigma^2 (n-j)} \sum_{i=1}^{n-j} (X_i - \mu)(X_{i+j} - \mu) \quad [3]$$

where $j = 0,1,\dots, n-1$ with *n* being the number of data points, $\tau_j = j\Delta\tau$ is the lag distance between the two points in question where $\Delta\tau$ is the distance between two adjacent points, μ is the estimated mean, σ is the standard deviation and *X* is the random soil property. A Markov correlation function [41,44] was used to approximate the spatial correlation structure, see Eq. (4). The Markov function, which assumes that the correlation between two points decreases exponentially with distance was then fitted to the estimated correlation structure obtained from Eq. (3). This was accomplished by minimising the scale of fluctuation, θ, until the difference between $\hat{\rho}(\tau)$ and $\rho(\tau)$ was negligible, see Fig. 4. A vertical scale of fluctuation of 1.424 m with a 95% confidence interval of {1.403 m, 1.445 m} was determined for the 23m deep sand layer (from 0 to 23m in Fig. 2) in the Port of Rotterdam and 1.771 m with a 95% confidence interval of {1.735 m, 1.807 m} for the bottom layer .

$$\rho(\tau_j) = \exp\left(\frac{-2|\tau_j|}{\theta}\right) \quad [4]$$

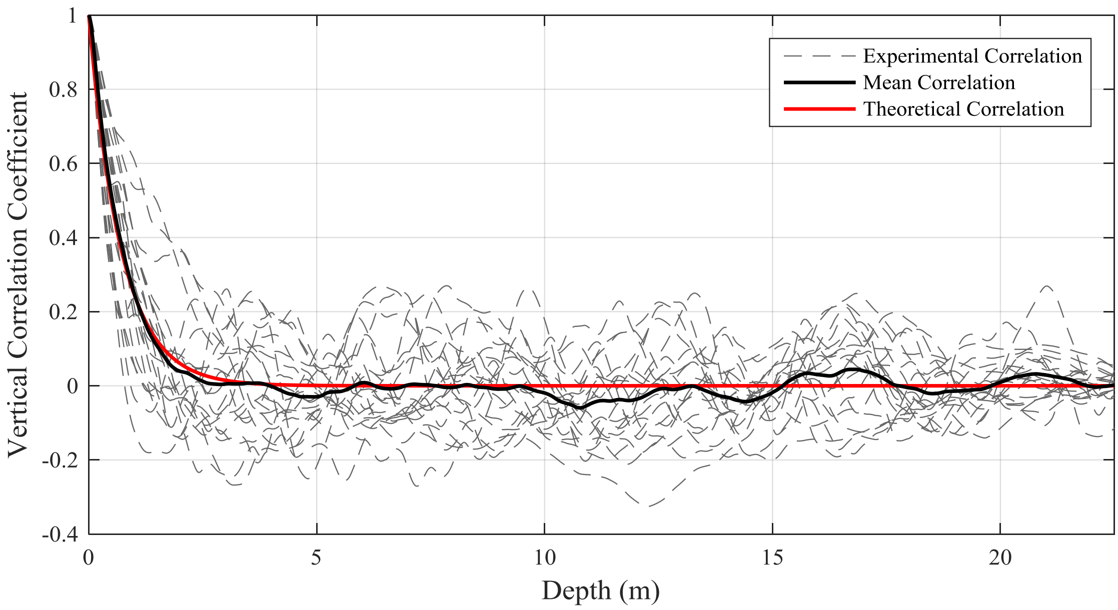

Fig. 4 Estimated vertical correlation structure from 20 CPTs and fitted theoretical correlation function using a 1.424m scale of fluctuation for top layer.

The resulting correlation matrix ρ is positive definite and can be decomposed into upper $\mathbf{L}^{\mathbf{T}}$ and lower $\mathbf{L}$ triangular forms using Cholesky Decomposition, see Eq. (5).

$$\boldsymbol{\rho} = \mathbf{L}\mathbf{L}^{\mathbf{T}} \quad [5]$$

The correlated matrix of normalised random processes, **G**, is then obtained by multiplying the lower triangular matrix with **U**, a vector of 50,000 independent normal random numbers with zero mean and unit standard deviation per depth increment, see Eq. (6).

$$\mathbf{G} = \mathbf{L}\mathbf{U} \quad [6]$$

If a normal distribution is required **G** can be inserted directly into Eq. (1), however in this paper, a lognormal distribution was used, as it demonstrated a better fit than the normal distribution and prevented negative tip resistance values from being generated, as these are physically inadmissible [45,46]. Note, a bounded normal distribution or a Beta distribution could also have been used. To generate a lognormally distributed random processes, the mean and standard deviation first need to be transformed into the lognormal domain, see Eqs. (7) & (8).

$$\sigma_{\ln} = \sqrt{\ln\left(1+\sigma^2\right)} \quad [7]$$

$$\mu_{\ln} = \ln \mu - \frac{1}{2}\sigma_{\ln}{}^2 \quad [8]$$

The spatially correlated lognormally distributed random process is then obtained using Eq. (9).

$$\mathbf{q_c} = \exp\left(\mu_{\ln} + \sigma_{\ln}\mathbf{G}\right) \quad [9]$$

The calculations in this paper were carried out using 50,000 random spatially correlated CPT profiles generated using the methodology presented in Eqs. (4)-(9). The mean profiles used to generate these CPTs is shown in Fig. 5 (Rotterdam Harbour CPT data), with the standard deviation calculated per CPT and averaged over each layer. The previously evaluated vertical scale of fluctuation of 1.424 m (for the top layer) and 1.771 (for the bottom layer) was used.

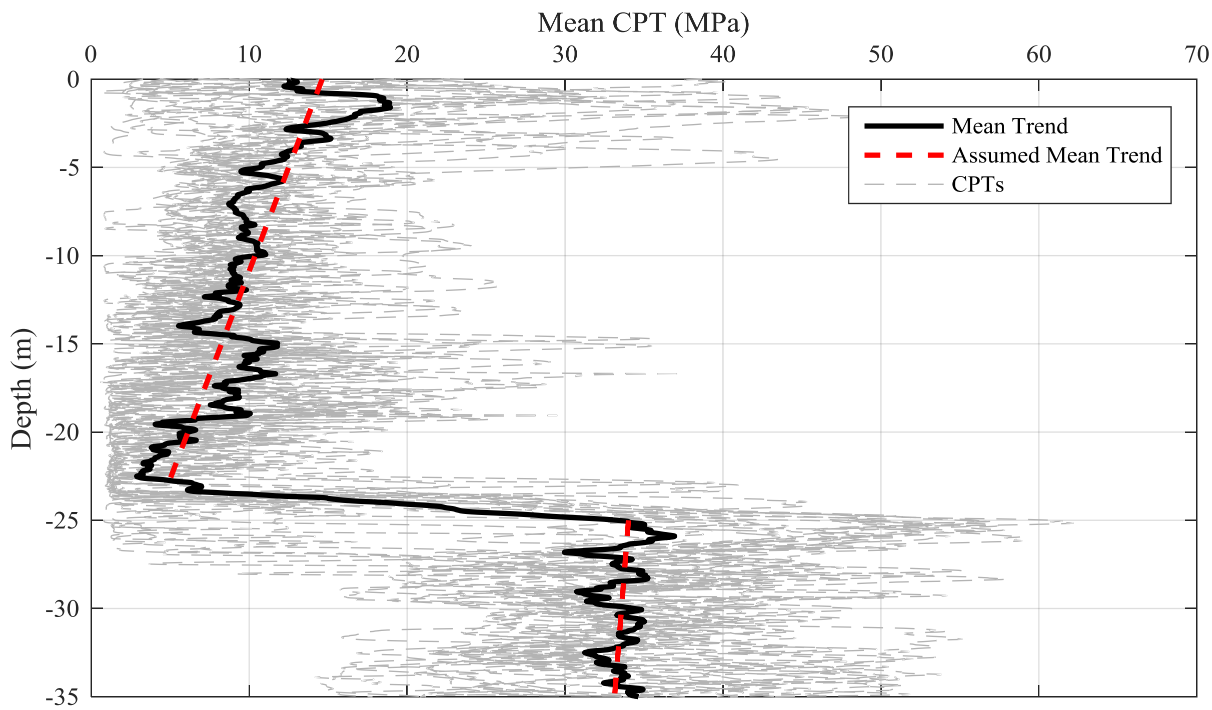

Fig. 5 The 20 CPT profiles with assumed mean trend for determining spatial variation and subsequently generating a random process model for the soil layers

4.0 Wind turbine model

A numerical model of a wind turbine was developed using 1-D finite elements (FE). The properties of the model were initially derived based on the recommendations in Sørensen and Ibsen [13], who state that monopiles supporting wind turbines have typical diameters of D=4-5m, wall thicknesses of 50-120mm and penetrations of L=15-30m. They currently support 2-5MW turbines in 10-25m water depths. The model used in the present study consists of a 6m diameter monopile [26], with an overall length of 75m (water depth of 30m) and an embedded length of 30m (L/D = 5). The embedded length was derived using the Critical Pile Length Criterion, described in Arany et al. [3]. The pile supports a 70m high tower and nacelle assembly, see Fig. 6. A pile wall thickness of 0.08 m was adopted as the cross-sectional properties of the monopile were tailored to the required design protocols (see section 4.2). The primary geometric and material properties adopted are outlined in Table 1.

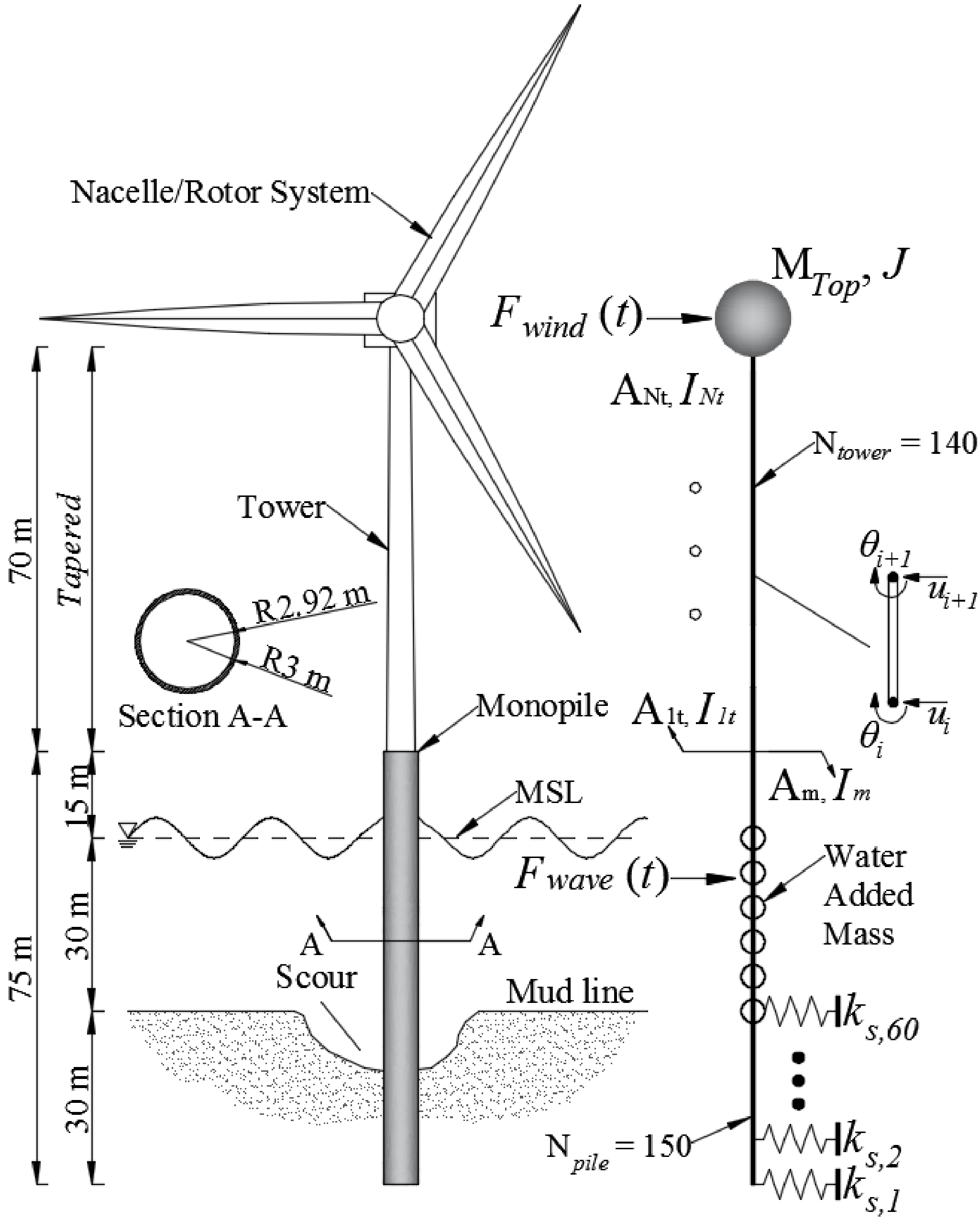

Fig. 6 Wind turbine model schematic.

4.1 Structural modelling

The monopile and tower were formulated numerically using four degree of freedom (4-DOF) Euler-Bernoulli beam elements, the elemental stiffness $\mathbf{K_i}$ and mass $\mathbf{M_i}$ matrices are available in Kwon and Bang [47]. Each element is 0.5m in length. Table 1 provides the primary material and geometrical information. The mass of soil within the monopile is treated as an added mass, by increasing the effective cross-sectional area of the elements below the mudline. A bulk unit weight of 20 kN m^{-3} is assumed for the internal soil. For the portion of the pile under water, hydrodynamic (external) and entrapped (internal) water added mass is incorporated using Eq.(10).

$$m_w = C_a \rho_w \frac{\pi D^2}{4} H \qquad [10]$$

where m_w is the added mass acting over the entire water column height, H, ρ_w is the density of sea water (1025 kg m^{-3}) and C_a is the coefficient of added mass multiplying the area of fluid displaced by the monopile. A value of C_a=2 is adopted, 1 for the external mass [48] and 1 for the internal mass [49]. Water added mass is formulated using an effective cross-sectional area for the elements below the water-line. All submerged elements are formulated using buoyant densities (ρ-ρ_w). Relative changes in added mass due to tidal action are not considered in the present study.

The tower is assumed to taper from a diameter of 5m at the base to 3.5m at the top so the cross-sectional area, *A* and moment of inertia, *I* vary along its length, as indicated in Table 1. The nacelle and rotor/blades system is modelled as a lumped mass at the top of the tower, formulated by adding a lumped mass matrix to the final beam element at the tower top, shown in Eq.(11). Eccentricities due to the offset of the nacelle mass from the vertical, gyroscopic motion of the blades and aerodynamic damping are not considered in this study.

$$\mathbf{M_N} = \mathbf{M}_i + \begin{bmatrix} 0 & 0 & 0 & 0 \\ 0 & 0 & 0 & 0 \\ 0 & 0 & M_{nacelle} & 0 \\ 0 & 0 & 0 & J \end{bmatrix} \qquad [11]$$

where $M_{nacelle}$ is the mass of the nacelle (kg) taken as 230,000 kg [50] and *J* is the rotational inertia in the fore-aft direction (kg m^2) taken as 3.5×10^7 kg m^2. The soil dynamic stiffness is incorporated using Winkler spring elements [26,51–54], with linear stiffness. It is assumed that the soil springs have a null mass matrix.

The discrete spring stiffnesses are derived from the stochastic soil model, see section 4.2 for a discussion on the derivation of soil spring stiffness (geotechnical) for the present study. The various local elemental matrices are assembled into global (*n* x *n*) mass and stiffness matrices [47] for the full system and the undamped natural frequencies and mode shapes are obtained by solving the eigen-problem shown in Eq.(12).

$$\left([\mathbf{M}^{-1}\mathbf{K}] - \lambda[\mathbf{I}]\right)\{\mathbf{A}\} = \{\mathbf{0}\} \qquad [12]$$

where $[\mathbf{I}]$ is the identity matrix, $[\mathbf{M}^{-1}\mathbf{K}] - \lambda[\mathbf{I}]$ is the characteristic matrix, $\lambda = \omega_n^{\ 2}$ are the eigenvalues and $\{\mathbf{A}\}$ the associated eigenvectors. The eigenvalues and eigenvectors (natural frequencies and mode shapes) are obtained by solving the characteristic equation. In total the model is formulated using 140 elements for the tower (height = 70m), 150 elements for the monopile (length = 75m) and 60 springs for the un-scoured soil profile (depth of embedment of 30m). A water depth of 30m with 15m freeboard is assumed [26]. The scour process is modelled in the numerical model as the iterative removal of springs starting at the top (removing the apportioned spring stiffness from the assembled global stiffness matrix), corresponding to an increase in scour depth equating to the FE length discretisation, L.

Table 1 Model Properties

Tower/Nacelle Properties:	**Value:**	**Monopile Properties:**	**Value:**
Tower length (m)	70	Monopile length (m)	75
Material	Steel	Embedded length (m)	30
Density (kg m^{-3})	7850	Material	Steel
Young's modulus (GPa)	210	Density (kg m^{-3})	7850
Tower diameter (m)	5 – 3.5	Young's modulus (GPa)	200
Tower wall thickness (m)	0.045	Monopile diameter (m)	6
X-sectional area (A_{it}) (m^2)	0.7005-0.4884	Monopile wall thickness (m)	0.08
Moment of inertia (I_{it}) (m^4)	2.15-0.7289	X-sectional area (A_m) (m^2)	1.4879
Nacelle/Rotor mass (M_{Top}) (kg)	230,000	Moment of inertia (I_m) (m^4)	6.5192
Nacelle rotational inertia fore-aft direction (J) (kg m^2)	3.5 x 10^7	Mass of power unit at interface level ($M_{Transition}$) (kg)	27,000

4.2 Geotechnical modelling

Arany et al. [3] present a step-by-step monopile design procedure covering the Ultimate Limit State (ULS), Serviceability Limit State (SLS), Fatigue limit State (FLS), Target Natural Frequency (TNF) and Installation Criteria. The purpose of the present paper is to highlight how geotechnical uncertainty and spatial variability in soil strength combined with scour erosion can affect a wind turbine's system frequencies. Therefore, the TNF design is the most important to ensure design compliance for the given ground conditions. Once the TNF is evaluated, basic SLS checks are undertaken to ensure compliance against the wind and wave environment. Section 4.2.1 discusses the basis for simple wind and wave loading calculations, section 4.2.2 describes how the soil-structure interaction for the scour modelling is incorporated, section 4.2.3 presents an overview of the TNF analysis and section 4.2.4 presents the compliance checks for the SLS for the derived model properties. Note, only the minimum design checks are conducted in this paper, a full design should consider ULS, SLS, FLS, TNF, driveability and buckling, among others.

4.2.1 Load basis for pile design

For compliance checking of the monopile in SLS, a baseline load estimation is required. Note, the loading for SLS is assumed as that applied under normal turbine operating conditions. Extreme loads for ULS calculations are not considered, as their effect on serviceability is assumed negligible since they will not occur very often. Interested readers are directed to Arany et al. [3] for a more in-depth load calculation basis. The recommendations of Corciulo et al. [49] are adopted herein, which describes a simplified wind/wave loading regime. The assumptions are that wind and wave thrusts, F_{wind} and F_{wave} (i) depend on wind velocity and system geometry, (ii) depend on the application of empirical aero- and hydrodynamic factors and (iii) are co-directional. Also, the effect of rotor revolution on wind speed is neglected. Wind thrust can be calculated according to Eq.(13).

$$F_{wind} = \frac{1}{2} A_R C_T \rho_{air} V_{wind}^2 \qquad [13]$$

where A_R is the swept area of the rotor (m^2), ρ_{air} = 1.2 kg m^{-3}, V_{wind} is the wind speed (m s^{-1}) and C_T = 0.688 (empirical wind thrust coefficient). By postulating a sustained wind field, an equilibrium sea state is assumed. A Pierson-Moskowitz wave spectrum [55] is postulated to quantify the wave energy *S* associated with each frequency *f*, see Eq.(14).

$$S(f) = \frac{\alpha g^2}{(2\pi f)^5} \exp\left[-\beta \left(\frac{g}{2\pi f V_{wind}^{19.5m}} \right)^4 \right] \qquad [14]$$

where α=0.0081 and β=0.74 are empirical constants, g=9.81 m s^{-2}, $V_{wind}^{19.5m}$ = wind speed at 19.5m above sea level. Wind speeds can be extrapolated from a reference measurement using a power law formulation [56]. Wave frequency f_S (at maximum spectral amplitude) and wave height H_S (distance between crest and trough) are shown in Eq.(15).

$$f_S{}^4 = \frac{4\beta}{5} \left(\frac{g}{2\pi V_{wind}^{19.5m}} \right)^4 \qquad [15a]$$

$$H_S = 2\sqrt{\frac{\alpha}{\beta}} \frac{\left(V_{wind}^{19.5m}\right)^2}{g} \qquad [15b]$$

The mono-harmonic sea state defined by f_S and H_S can be transformed to a hydrodynamic thrust F_{wave} using the Morison equation [57], with drag and inertial force components as shown in Eq.(16).

$$F_{wave}^{DRAG} = \rho_w g \frac{C_d D}{8} H_S^2 \left(\frac{1}{2} + \frac{kH}{\sinh 2kH} \right) \quad [16a]$$

$$F_{wave}^{INERTIA} = \rho_w g \frac{C_m \pi D^2}{8} H_S \tanh kH \quad [16b]$$

The overturning moments with respect to the mudline are shown in Eq.(17).

$$M_{wave}^{DRAG} = \rho_w g \frac{C_d D}{8} H_S^2 \left[\frac{H}{2} + \frac{2(kH)^2 + 1 - \cosh 2kH}{4k \sinh 2kH} \right] \quad [17a]$$

$$M_{wave}^{INERTIA} = \rho_w g \frac{C_m \pi D^2}{8} H_S H \left[\tanh kH + \frac{1}{kH} \left(\frac{1}{\cosh kH - 1} \right) \right] \quad [17b]$$

C_d and C_m, the drag and inertia coefficients are taken as 0.65 and 1.6 respectively. *H* is the height of the water column (m), *D* is the monopile diameter (m), ρ_w is the seawater density (1025 kg m^{-3}) and k is the wave number, related to the wave length (λ_w) by $k = 2\pi / \lambda_w$ [58]. *k* can be obtained from the dispersion relation [3], shown in Eq.(18).

$$\omega^2 = gk \tanh(kH) \quad [18]$$

where $\omega = 2\pi f_S$. Eq.(18) is an implicit equation, therefore solutions must be found numerically. However, an explicit approximation may be obtained by Eq.(19) [59].

$$k = \frac{\omega^2}{\left[g \left[\tanh \left\{ \left(\frac{2\pi \sqrt{\frac{H}{g}}}{T} \right)^{\frac{3}{2}} \right\} \right]^{\frac{2}{3}} \right]} \quad [19]$$

where $T = 2\pi / \omega$. The drag and inertial components of the wave thrust will be out of phase, therefore resultant mudline forces and moments are calculated using the Square Root Sum of Squares (SRSS)[58], see Eq.(20).

$$F_{wave} = \sqrt{\left(F_{wave}^{INERTIA}\right)^2 + \left(F_{wave}^{DRAG}\right)^2} \quad [20a]$$

$$M_{wave} = \sqrt{\left(M_{wave}^{INERTIA}\right)^2 + \left(M_{wave}^{DRAG}\right)^2} \quad [20b]$$

It is assumed that the sustained wind speed under normal turbine operating conditions in combination with associated wave loading is the critical load scenario for SLS design compliance in this paper. The wind turbine modelled is a 3.6MW turbine [50], with nominal power production at a wind speed of 12 m s^{-1}. The derived unfactored wind and wave loads used in this paper are show in Table 2.

Table 2 loading for SLS compliance

V_{wind}	$V_{wind}^{19.5m}$	F_{wind}	Lever Arm	F_{wave}	M_{wind}	M_{wave}	Mudline *F*	Mudline *M*
m s^{-1}	m s^{-1}	kN	m	kN	kNm	kNm	kN	kNm
12	10.05	670	115	480	77050	15980	1155	93225

4.2.2 Soil-Structure Interaction

The soil-structure interaction between the monopile and the surrounding soil is incorporated via the Winkler hypothesis [51], using an array of discrete, mutually independent, 1-D spring elements. For the purpose of sizing the monopile, the design spring stiffness was derived from the average CPT q_c profile in Fig. 2. Linear springs were used for the small-strain TNF analysis, and non-linear springs were derived for the SLS check.

When the system parameters were adequately sized, the effect of spatial variability and geotechnical uncertainty on system natural frequencies for various scour depths was assessed. For this analysis, small-strain linear springs were developed from the randomly generated, spatially correlated ground profile.

The process of calculating individual spring moduli is discussed herein. A hypothetical CPT profile developed using the stochastic ground model is converted to small-strain linear springs distributed along the monopile shaft. Each CPT profile is discretised into 0.5m depth increments (to correspond to the discretisation in the FE model) and each increment is transformed to the small-strain shear modulus (G_0) using Eq.(21). In the absence of laboratory or geophysical measurements of G_0 [53,60], correlations between G_0 and q_c developed by Lunne et al.[61] and Schnaid et al.[62] have been shown to provide reasonable estimates of the small strain stiffness response when the stress history, age and degree of cementation is considered. By taking the average q_c profile for the site (Fig. 2) and assuming a 30m embedded monopile the relationship proposed by Schnaid et al. [62] suggest a value of n = 6 is appropriate for this deposit. This is within the expected range for dense sands.

$$G_0 = nq_c \quad [21]$$

The small-strain shear modulus G_0 profile can be converted to a profile of the small-strain Young's modulus according to $E_0 = 2G_0(1+v)$, where v is the small-strain Poisson ratio. The modulus of subgrade reaction (K) can then be derived using the procedure outlined in [12,26,63] (originally developed by Vesic [64]), see Eq. (22).

$$K = \frac{E_0}{1-v^2}\left[\frac{E_0 D^4}{E_p I_p}\right]^{1/12} \qquad [22]$$

where E_p and I_p are the Young's modulus and moment of inertia of the pile, respectively. K is subsequently converted to individual spring moduli ($k_{s,i}$) by multiplying the K profile at a given depth by the distance between subsequent springs (L), at each spring depth.

Deriving soil-structure interface stiffness using this method has been shown to be accurate in experimental studies previously conducted. Prendergast and Gavin [53] performed experimental vibration tests on two piles with varying slenderness ratios (L/D) in dense sand and compared the results to numerical models developed employing five different modulus of subgrade reaction formulations. The model employing the Vesic formulation [64], a variation on Eq. (22) provided the closest approximation of the natural frequencies for both piles tested. Moreover, Prendergast et al.[12,26] derived soil stiffness profiles using Eq. (22) from shear wave velocity and CPT measurements and compared experimental results to numerical models at modelling the change in frequency due to scour. In one study [12], a pile with L/D of 19 was used and in the second [26], a pile with L/D of 6.5 was used. For both cases, the stiffness derived using Eq. (22) proved accurate at tracking the frequency changes due to scour imposed on the physical systems. Ashford and Juirnarongrit [63] performed a study to evaluate the effect of pile diameter on the initial modulus of subgrade reaction. They derived the subgrade reaction using Eq. (22) and compared numerical models to experimental piles with diameters of 0.4m, 0.6m, 0.9m and 1.2m. The study concluded that models employing Eq. (22) were capable of estimating the natural frequencies of each system to within a ratio of 0.98 to 1.04 times the measured values.

4.2.3 Target Natural Frequency (TNF)

Unlike other large civil structures such as oil and gas platforms, offshore wind turbines are particularly dynamically sensitive [26]. An over or under prediction in the system frequency can be detrimental to the stability and fatigue life of these structures in operation. The system is subjected to periodic loading from a number of sources including wind and wave as well as those arising due to the operation of the turbine. The frequency generated by the rotational velocity of the rotor is termed the 1P frequency [3,6,26]. A further loading frequency is generated due to the turbulent interaction when the blades pass the tower (shadowing effect), termed the N_bP frequency, where N_b is equal to the number of blades on the turbine. Wind loading occurs with typical frequencies lower than the 1P frequency. Fig. 7(a) shows nominal ranges for the 1P and 3P frequencies of the turbine modelled in this paper [50], along with the Pierson-Moskowitz wave spectrum. The wind spectrum is omitted. PSD magnitudes are normalised for illustrative purposes. The 1P and 3P frequency ranges represent the lowest and highest revolutions per minute (RPM) of the rotor [3,50] (5-13 RPM). For monopile supported turbines, typical design frequencies reside in the soft-stiff range, between the 1P and 3P bands. It is first necessary to size the tower assuming it is clamped at the bottom (fully fixed and no monopile). The clamped first frequency for a soft-stiff founded system should be close to 0.5Hz [65]. Using this threshold, a 70m long tower with a tapering diameter of 5m (base) to 3.5m (top), average diameter 4.25m, yields a frequency of 0.496 Hz (≈0.5 Hz). When connected to the monopile, the whole system should have a frequency in the range 0.28-0.31 Hz. A 6m diameter monopile with a wall thickness of 80 mm provides a first natural system frequency of 0.3012 Hz and a second in-plane bending frequency of 1.1331 Hz, using the design average CPT profile from Fig. 2 and incorporating water added mass. The second in-plane bending frequency equates to the third mode of vibration, as the second mode will be out of plane and very close in value to the first frequency for symmetrical structures, see Fig.7(b) for mode shapes. Note, that the first natural frequency resides in the tail of the 3P band. This is not an issue, however, as the nominal operating RPM will typically be at the upper end of the range, therefore resonance due to blade shadowing at this low rotational velocity is not expected (and can be avoided using the control system of the turbine). The following section describes the serviceability check undertaken to ensure the chosen pile dimensions are compliant with wind and wave loading.

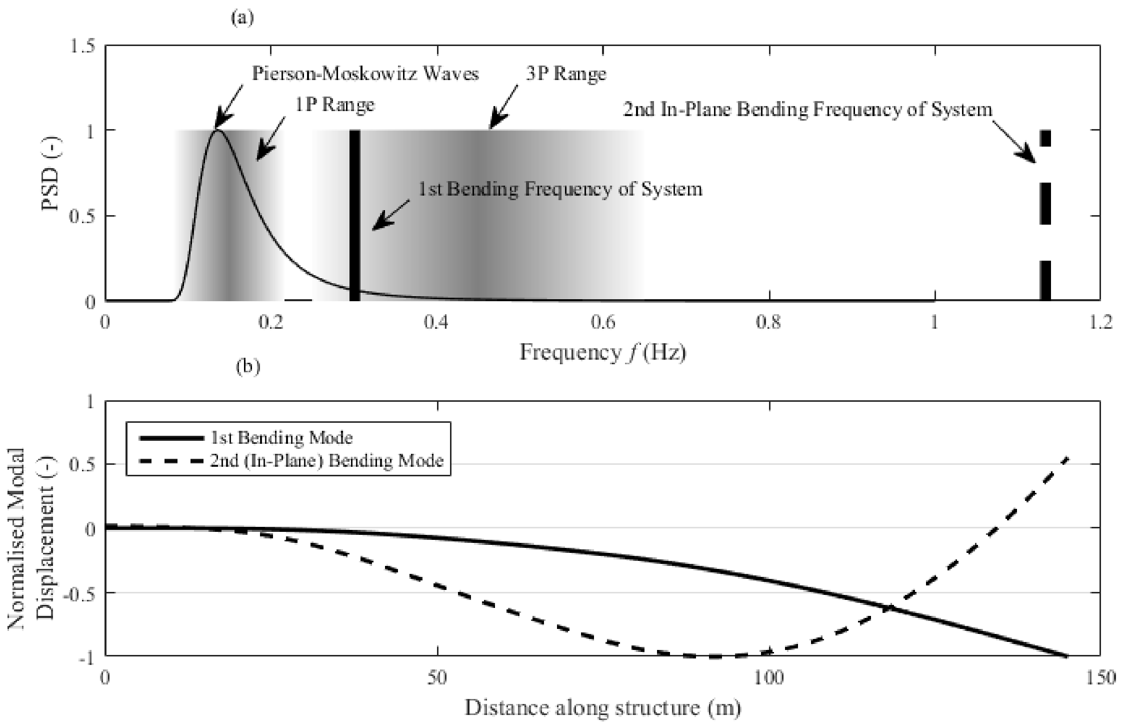

Fig. 7 (a) Frequency bands for present system, (b) First and second in-plane bending mode shapes

4.2.4 Serviceability Limit State (SLS)

Basic SLS checks are carried out to ensure model compliance with accepted thresholds. The allowable accumulated mudline rotation over the lifetime of a wind turbine founded on a monopile is normally limited to 0.25° rotation, in addition to an initial allowable tilt of 0.25° at the mudline to allow for errors upon installation of the pile [3]. Furthermore, the initial mudline deflection is limited to 0.2m as is the accumulated deflection over the lifetime of the system [3].

To perform preliminary checks, a nonlinear *p-y* analysis was carried out using a finite-difference solver, whereby the pile is modelled using linear beam elements and the soil is modelled as a series of discrete, nonlinear *p-y* springs. Two approaches are used to generate *p-y* springs for this study, the American Petroleum Institute (API) method [66] and a CPT-based approach for piles in sand [67].

The API design code for laterally loaded piles in sand characterises soil spring *p-y* relation as a hyperbolic function, as shown in Eq.(23) [8,11]. It was originally derived based on a database of lateral load tests on piles with relatively high slenderness ratios [8].

$$p = Ap_u \tanh\left(\frac{kz}{Ap_u}y\right) \qquad [23]$$

where p_u is the ultimate resistance at depth ‘z’ below the ground surface (kN m^{-1}), k is the constant coefficient of subgrade reaction (kN m^{-3}), A is an empirical factor accounting for static or cyclic external loading and y is the lateral deflection (m). Numeric values for k are specified in the API design code [66], and depend on the friction angle or density of the soil and vary for saturated and unsaturated conditions. For the analysis in this paper, API springs were generated based on a design friction angle profile, derived using the average CPT profile from Fig. 2. The average CPT profile was converted to a profile of the angle of internal friction using a relation from Kulhawy and Mayne [68], shown in Eq.(24). The design profile was then obtained by discretising this profile into layers, see Fig. 8(b).

$$\varphi = 17.6 + 11\log\left[\left(\frac{q_c}{\sigma_{atm}}\right)/\left(\frac{\sigma'_{v0}}{\sigma_{atm}}\right)\right]^{0.5} \qquad [24]$$

where σ'_{v0} is the effective stress (kN m^{-2}) and σ_{atm} is the atmospheric pressure (taken as 100 kN m^{-2}). The CPT-based approach is based on Suryasentana and Lehane [67], who described a *p-y* curve derivation technique for laterally loaded piles in sands, which may be more applicable to the rigid pile geometries used in the offshore wind sector. They propose an exponential relationship for the *p*-*y* curves, shown in Eq. (25).

$$\frac{p}{\gamma z D} = 2.4\left(\frac{q_c}{\gamma z}\right)^{0.67}\left(\frac{z}{D}\right)^{0.75}\left\{1-\exp\left[-6.2\left(\frac{z}{D}\right)^{-1.2}\left(\frac{y}{D}\right)^{0.89}\right]\right\} \quad [25]$$

where p is the soil reaction at a given spring depth (kN m^{-1}), γ is the bulk unit weight of the soil (kN m^{-3}), z is the depth to the middle of each design layer (m), D is the monopile diameter (m) and y is the lateral deflection (m).

The design profiles used for both methods are shown in Fig. 8. Fig. 8(a) shows the average CPT profile from Rotterdam Harbour (section 2.0) and the layered averaged profile, used in the lateral load analysis for the CPT-based *p*-*y* approach. Fig. 8(b) shows the derived φ' profile and a depth averaged profile used in the API approach.

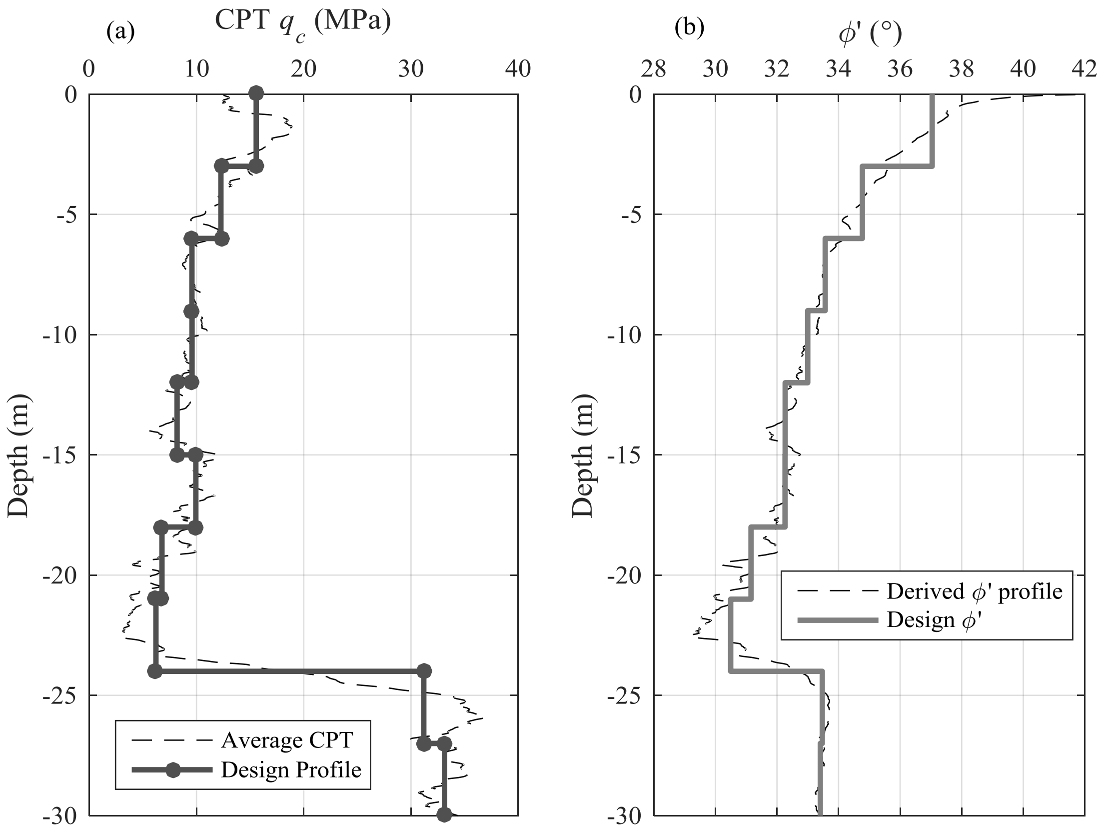

Fig. 8 Design profiles for SLS check, (a) Average and design CPT q_c profile, (b) Derived and design φ' profile

The analysis is conducted using a finite-difference program that solves for the pile head lateral displacements and rotations under combined lateral and moment loading. The program operates by specifying an initial tangent stiffness for each *p-y* spring, solving for the displacement of the system under this operating stiffness and iteratively updating the spring stiffness of each spring according to the relationships specified in Eqs. (23) and (25). The analysis iterates until some predefined tolerance is achieved. The unfactored lateral load and moment at the mudline are shown in Table 2, as derived from the wind and wave loading calculations. These loads are factored by 1.5 and applied to the pile at mudline. The load-displacement and moment-rotation response curves from both *p-y* approaches are shown in Fig. 9. The results are broadly in agreement with the API approach predicting a lower lateral stiffness than the CPT-based approach in the initial stages. This finding is in agreement with Kallehave and Thilsted [69] who note that the API method can under predict stiffness for rigid piles, though for the present case this error is minor. As per the limits in Arany et al. [3], a threshold rotation of 0.25° or pile head displacement of 0.2m is permitted for fundamental SLS checks. Both displacement and rotation are well within the required bounds for both checks. Note, only fundamental SLS checks are considered, the plastic accumulation in rotation was not calculated.

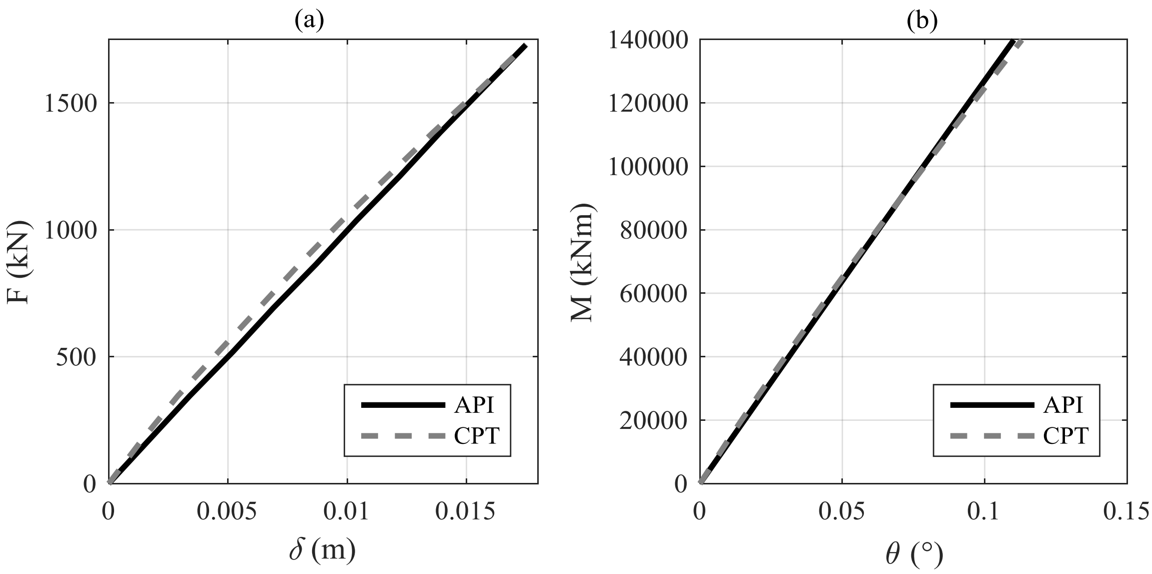

Fig. 9 SLS Checks for API and CPT-based approach, (a) Load-Displacement, (b) Moment-Rotation responses

5.0 Analysis & Results

In this paper, the statistical variation in potential frequency changes due to scour incorporating spatial variability in soil strength is investigated. From the twenty CPT profiles measured at Rotterdam Harbour, a total of 50,000 hypothetical profiles are generated based on the process outlined in section 3.0. A Monte-Carlo simulation is carried out whereby each hypothetical CPT profile is converted to a profile of spring coefficients using the procedure discussed previously and then assembled into the global matrices of the turbine structural model using the procedure in section 4.1. The analysis outputs likely frequency values (first and second in-plane natural system frequency) for each hypothesised ground profile. The design scour depth for an offshore monopile as recommended by DNV [70] is 1.3 pile diameters (1.3D), though this is based on current-only flow conditions. Physically there is little merit to this limit as in marine environments, the combined action of currents, tides and waves can give rise to significantly more complex interactive behaviour [14], where scour temporal variation could exceed this threshold. In this paper, scour depths ranging from 0m to 10m (1.66D) in discrete depths of 0.5m are implemented in the model by iteratively removing springs and the likely output frequencies due to each profile is calculated at each scour depth. Fig. 10 shows a histogram of the resulting output first natural system frequency values obtained at zero scour, 5m scour and 10m scour depths.

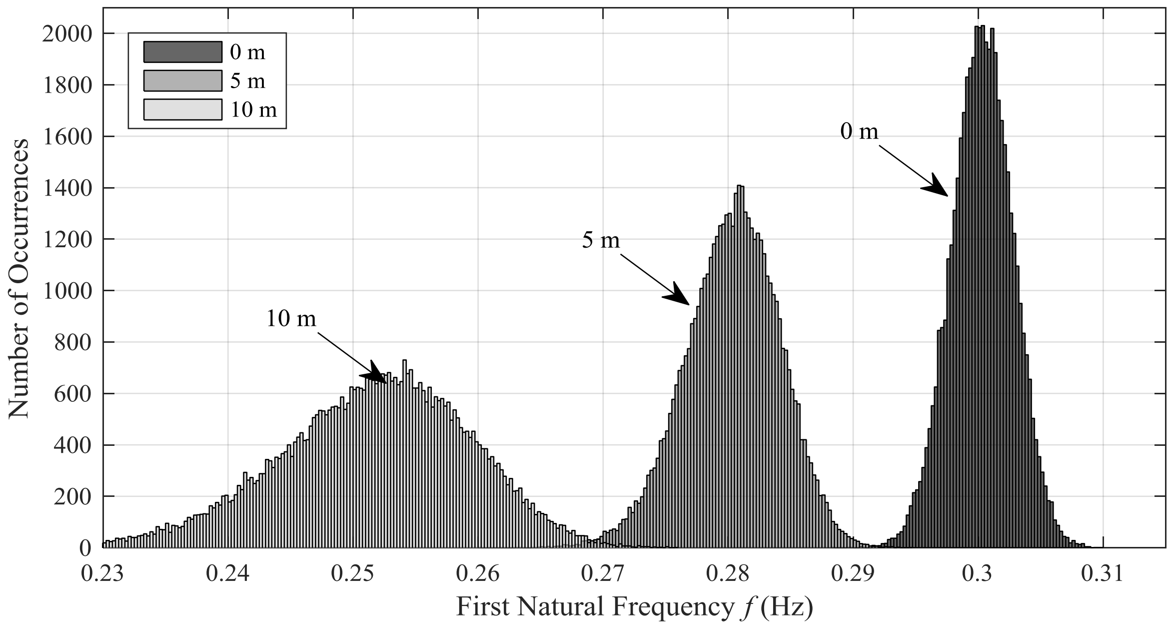

Fig. 10 Number of occurrence of first natural frequency for 0, 5 and 10 m scour depths

It is evident from the results in Fig.10 that the first natural system frequency reduces as the scour depth increases. A striking feature of the data is that the range (spread) of predicted system frequencies also increases as the scour progresses. This is a result of the increased flexibility of the overall system as scour progresses causing a larger relative change in frequency for a given range of hypothesised ground profiles. This trend is readily observed in Fig. 11(a), which shows the change in mean first natural frequency plotted again the depth of scour. The mean frequency is obtained at each scour depth from the distribution of outputs. Also shown in Fig. 11(a) are the envelopes of the change in frequency with scour at one and two standard deviations away from the mean at each scour depth. It may be observed that the standard deviation moves further away from the mean profile with increased scour depth, which mimics the response observed in Fig. 10. Fig.11(b) shows the same information but for the second in-plane bending frequency. The change in this frequency is more linear with depth, and the standard deviation still moves away from the mean with increased scour, though this is less obvious in this case. This indicates that the deeper the scour depth, the less certain one can be as to the actual depth of scour affecting the system, based solely on frequency measurements. However, the deeper the scour depth, the more certain one can be that some degree of scour is affecting the system. For example, if a frequency of 0.28 Hz is measured, this indicates a scour depth of just over 5m based solely on the mean. However if one considers two standard deviations either side of the mean frequency, a frequency of 0.28 Hz could indicate a potential scour depth of anywhere between 3.5m and 7m. For deeper scour, the potential variation is larger. The likelihood of a given scour depth existing under a detected frequency can be more coherently visualised by examining the cumulative distribution of the results, see Fig. 12.

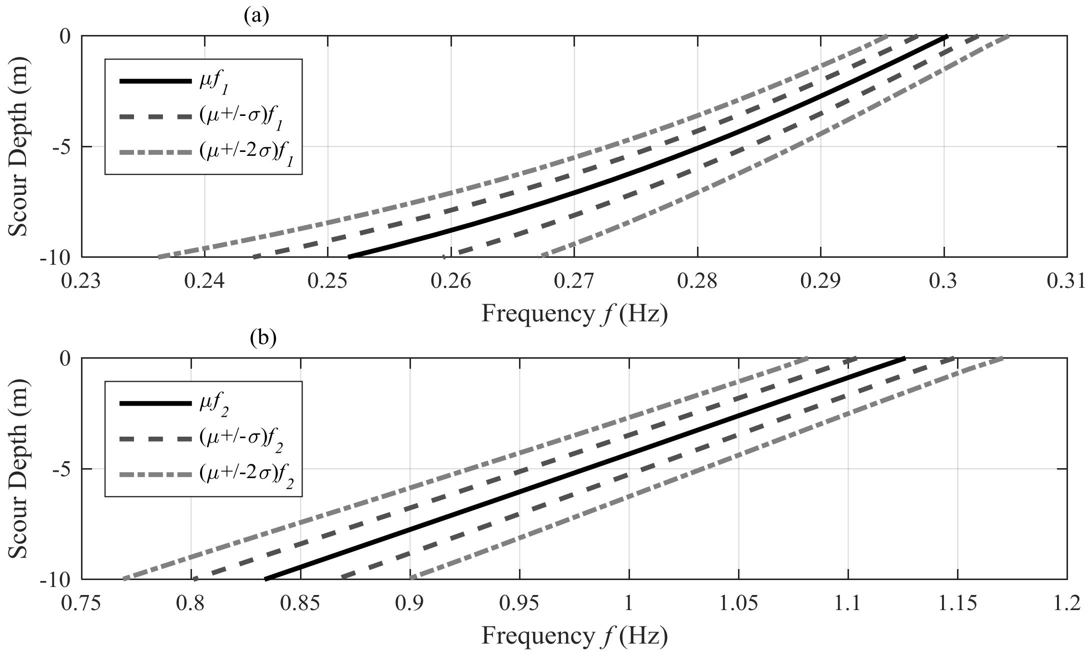

Fig. 11 Mean and standard deviations of frequencies vs. scour depth (a) first frequency, (b) second in-plane frequency

Fig. 12 shows the Cumulative Distribution Function (CDF) of the first natural frequency results for scour depths of 0 to 10m in 1m discrete depths (for clarity, the results at each 0.5 m depth increment are omitted from the figure). The results indicate the probability of scour being a certain depth or less for a given frequency measurement. For example, if a frequency of 0.28 Hz is measured, this indicates an almost 0% probability that the depth of scour is 3m or less, an 8% probability of 4m scour or less, a 44% probability of 5m scour or less, an 85% probability of 6m scour or less and almost 97% probability of 7m scour or less.

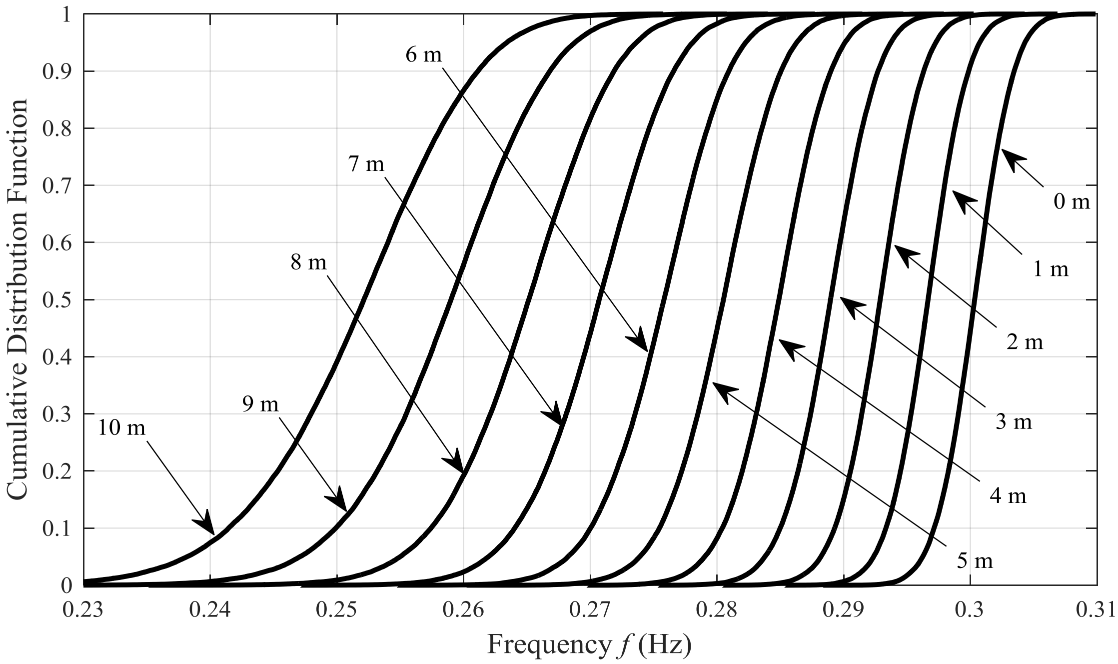

Fig. 12 Cumulative Distribution Function (CDF) of frequency with scour

As every scour depth has an associated frequency distribution and the initial shift in mean frequency when scour begins is not substantial, there is a considerable overlap between the "no scour" distribution and the "0.5 m scour" distribution, see Fig. 13. Therefore statistical tests were carried out to ensure that (i) the sampled distributions were not part of the same overall population and (ii) the change in frequency due to the scour was sufficient to ascertain the presence of scour.

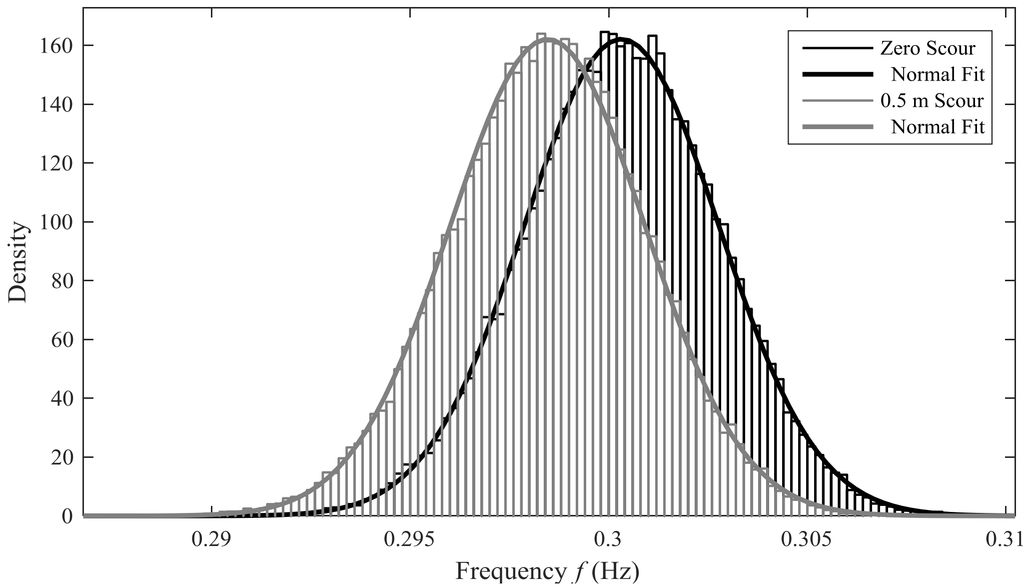

Fig. 13 Distribution of frequencies for zero scour and 0.5 scour affecting the structure

To determine if calculated sampled natural frequency distributions could come from the same population the Kruskal-Wallis test was used. This test is a non-parametric version of the classical one-way analysis of variance (ANOVA) approach, and is an extended form of the Mann-Whitney U-test allowing more than two groups to be tested at any one time. The test orders all the data from low to high and then utilises this data rank instead of numeric values to compute test statistics. A chi-square statistic is used along with a probability value (p) which measures its significance. A 5% significance level was adopted. The test determined that the difference between the median values for every scour interval (0.5m) was statistically significant and hence that no two distributions could be considered a subset of one another.

Fig. 14 shows the natural frequency plotted against scour depth with median values, interquartile ranges and outliers. In Fig.14, the red line in the middle of each blue box signifies the median value at a given scour depth, while the blue box represents the interquartile range. The whisker length represented by the dotted black line is set as 1.5 times the interquartile range and all outliers are shown as red crosses at each scour depth.

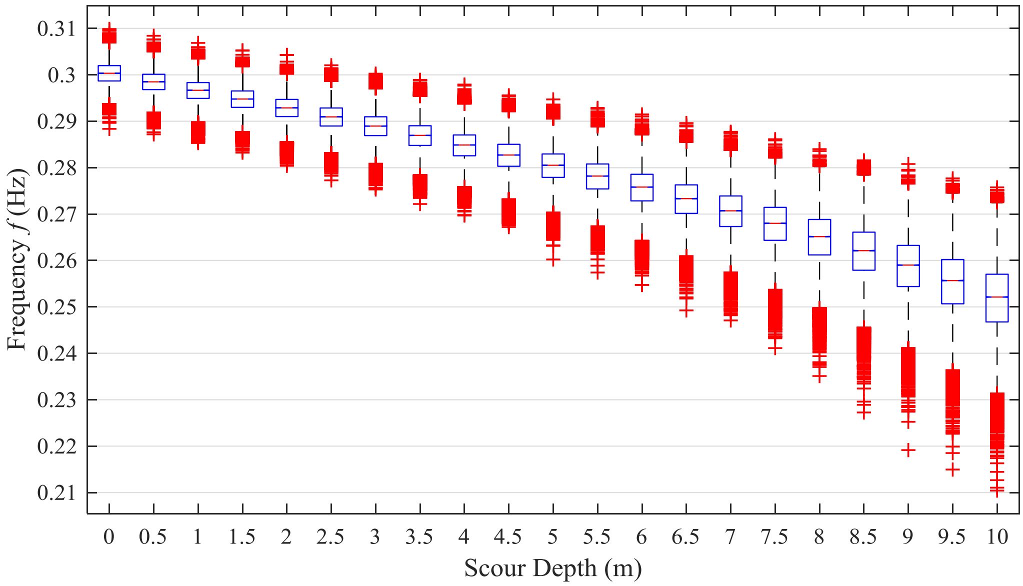

Fig.14 Box plot showing the difference in scour distribution with depth

It should be noted that while the computed frequencies were represented quite well by a normal fit for low scour depths, the distribution became less normal with increased scour, see Fig. 15. Fig. 15 shows the fitted normal distribution to the frequency data at 0m scour and 10m scour. The normal fit fits well for the zero scour case but the data is somewhat skewed for the 10m scour case. Strictly speaking the Kruskal-Wallis test assumes all parameters follow the same distribution. However, given that the deviation is small and occurs at a depth where scour is easily detectable through frequency change this can be considered acceptable.

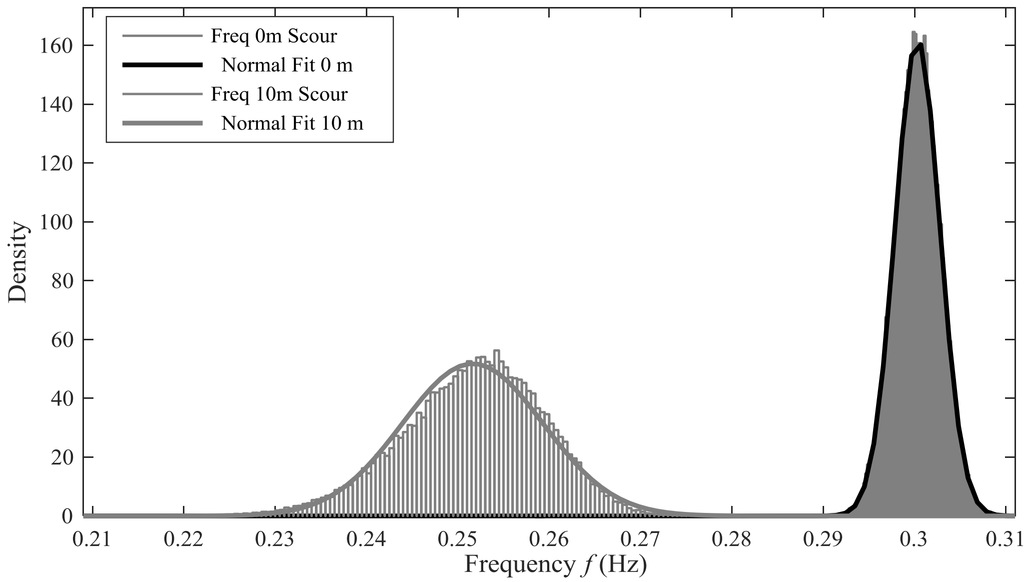

Fig.15 Frequency profiles become less normal with depth

The second test performed was the Receiver Operating Characteristic (ROC) Curve analysis, which is a test used to illustrate the ability of a system to classify itself between two outcomes as its discrimination threshold is varied. In the present case the ROC curve represents the diagnosis between scour and no scour for the overlapping frequency spectrum both outcomes could have. i.e. for any value where the distributions overlap there is a chance that scour is occurring and is classified as occurring (true positive), while there is also a chance that scour is occurring and is not detected (false negative). Similarly there is also a chance that no scour has occurred but is classified as having occurred (false positive) and finally a chance that no scour has occurred and is predicted as such (true negative). A ROC curve is therefore the sensitivity of the system expressed in terms of the probability of false alarm and thus represents the trade-off between a type 1 and type 2 error. Sensitivity is the probability that the test will indicate scour when it is present and specificity is the probability that the test will indicate that scour is not present when there is no scour.

A ROC curve consists of the true positive rate (Sensitivity) plotted against the false positive rate (1-Specificity) at different parameter criterion values. Each point on the curve corresponds to a sensitivity/specificity pair related to a particular decision. The area underneath the curve (AUC) represents how well one can differentiate between the two distributions in question, the closer AUC is to 1 the clearer the distinction. If there was no distribution overlap it would be impossible to identify a value as being from a distribution it is not. In such a case the ROC curve would follow the Sensitivity axis until it has reached one and would follow the 1-Specificity axis until it too has reached one. Therefore, the closer the apex of the curve is to the upper left hand corner the easier it is to distinguish whether a value comes from one distribution or another. The ROC curve analysis as applied to the present case is shown in Fig. 16. The "no scour" natural frequency distribution was compared using ROC curves to the following scour frequency distributions: (a) 0.5 m, (b) 1 m, (c) 1.5m and (d) 2 m. The resultant graphs shown in Fig. 16 show that for 0.5 m of scour, curve (a), there is a significant possibility of scour escaping detection (given the distance of the curve from the top and left-hand axis and its relatively poor sensitivity and specificity). However, for 1 m of scour, curve (b), this chance decreases substantially (denoted by the tendency of the apex to move closer to both axes as previously mentioned and the increase in Positive Predictive Value, PPV, Negative Predictive Value, NPV and AUC). For scour depths of 1.5 m, curve (c), and 2 m, curve (d), there is an excellent differentiation between the distributions for zero scour and the relevant scour depth and because of this delineation it is easy to distinguish whether or not scour exists for these depths and lower. Table 3 displays some values of interest resulting from this analysis. The PPV is the probability that there is a corresponding scour hole when scour is indicated, while the NPV is the probability that scour is *not* present when scour is *not* indicated. As evident, these probabilities increase with scour depth as the separation between the means of the no scour and scour distributions increases. When combined with the AUC these values allow us to gauge how reliably the model is predicting, while also informing how likely one is to predict a false positive (Type 1 error) or a false negative (Type II error).

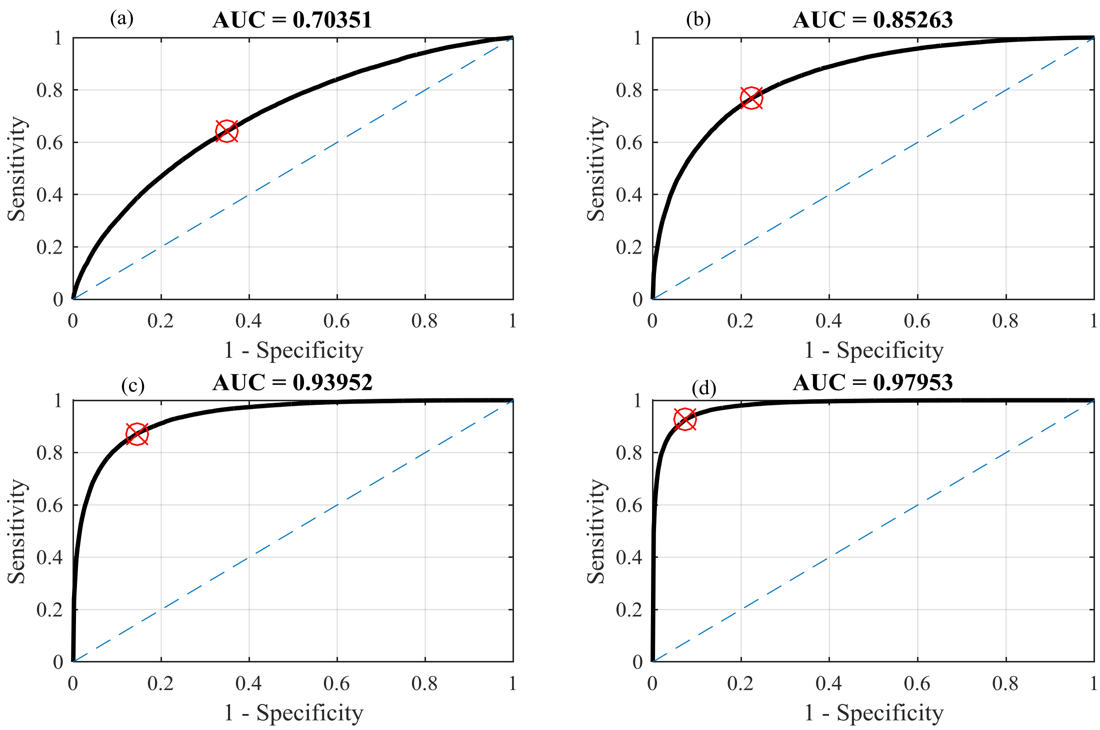

Fig. 16 ROC curves examining the ability to distinguish between the no scour frequency distribution and the frequency distributions corresponding to scour of (a) 0.5 m, (b) 1 m, (c) 1.5 m, (d) 2m.

Table 3 ROC Curve parameters

Scour Depth (m)	AUC	Positive Predictive Value PPV	Negative Predictive Value NPV	Sensitivity	Specificity
0.5	0.704	64.779 %	64.563 %	0.643	0.650
1	0.853	77.421 %	76.996 %	0.768	0.776
1.5	0.940	85.750 %	87.006 %	0.872	0.855
2	0.980	92.639 %	92.579 %	0.926	0.926

6.0 Concluding remarks

In this paper, the effect of spatial variability from CPT profiles and geotechnical uncertainty is investigated in terms of how it may affect the perceived natural frequencies of a wind turbine system in the context of using frequency changes due to scour in a SHM framework. Twenty Cone Penetration Test (CPT) tip resistance q_c profiles, measured at Rotterdam Harbour, were used to develop a stochastic ground model with spatially correlated strength properties. 50,000 hypothetical CPT profiles were generated representing likely profiles within the stochastic model and converted into operational soil-structure interaction stiffnesses for input into a Finite-Element model of a wind turbine.

A numerical model of a wind turbine founded on a monopile embedded in the soil was developed and eigen-analyses were conducted to calculate the first and second in-plane system natural frequencies of the turbine under progressive scour. The purpose of the model is to investigate the potential likely frequency variation that could exist due to likely operating soil stiffness profiles and to observe if the potential variation in frequency due to scour is larger than these potential variabilities. The question of how reliably scour can be detected and measured using a SHM regime is investigated.

The results indicate that significant variation in frequency at a given scour depth occurs using the stochastic ground model and as a result, a given frequency measurement gives rise to a relatively large band of potential scour depths. Moreover, there is increased variation in frequencies at a given scour level with increased scour progression. This is as a result of the increased bending flexibility of the system during scour and means it is more difficult to accurately detect the depth of scour as the scour depth increased. However, the large change in average frequency that occurs as scour progresses means that it becomes more certain that scour *exists*, even if the actual scour magnitude is more difficult to quantify. Due to the overlap present in the distributions of output frequencies, the use of ROC curve analysis to estimate the likelihood of detecting a false positive was investigated. The results indicate that for a low scour depth of 0.5 m there is significant likelihood of scour not being detected using frequency measurements. However, for deeper scour depths, the existence of scour is much more likely to be observed, even for relatively benign scour depths of 0.25D, in this case.

The analysis presented in this paper assumes that the only influence on the frequency of the turbine is the scour affecting the system. It is recognised that other factors will also influence the dynamics of the system such as cyclic loading, large strain soil deformation and soil stiffness degradation, tidal influence on water added mass, corrosion and other damage. The effect of measurement noise may also be a factor. For simplicity these are not considered in the present study and only the influence of scour erosion on the system frequencies is studied. The results in this paper are interesting in the context of the continued development of the offshore wind sector and remote scour monitoring fields and may be important with the development of larger systems in more uncertain design conditions. Future research will focus on the effect of scour on soil damping for offshore wind.

Acknowledgements

The research was partly funded by financial support from the European H2020 project SAFE-10-T (Project No. 723254) and Destination Rail (Project No. 636285) and the Department of Geoscience and Resource Engineering at TU Delft. The second author gratefully acknowledges the NVIDIA Corporation for the donation of a Tesla K40 GPU used in this research.

References

[1] EWEA. The European Offshore Wind Industry-Key Trends and Statistics. 2015.

[2] Negro V, López-Gutiérrez J-S, Esteban MD, Alberdi P, Imaz M, Serraclara J-M. Monopiles in offshore wind: Preliminary estimate of main dimensions. Ocean Eng 2017;133:253–61. doi:10.1016/j.oceaneng.2017.02.011.

[3] Arany L, Bhattacharya S, Macdonald J, Hogan SJ. Design of monopiles for offshore wind turbines in 10 steps. Soil Dyn Earthq Eng 2017;92:126–52. doi:10.1016/j.soildyn.2016.09.024.

[4] Byrne B, McAdam R, Burd H, Houlsby G, Martin C, Zdravković L, et al. New design methods for large diameter piles under lateral loading for offshore wind applications. Int. Symp. Front. Offshore Geotech., Oslo: 2015.

[5] Doherty P, Gavin K. Laterally loaded monopile design for offshore wind farms. Proc ICE - Energy 2012;165:7–17. doi:10.1680/ener.11.00003.

[6] LeBlanc C, Houlsby GT, Byrne BW. Response of stiff piles in sand to long-term cyclic lateral loading. Géotechnique 2010;60:79–90. doi:10.1680/geot.7.00196.

[7] LeBlanc C. Design of offshore wind turbine support structures. TU Denmark, 2004.

[8] Murchison JM, O'Neill MW. Evaluation of p-y relationships in cohesionless soils. Anal. Des. Pile Found. Proc. a Symp. conjunction with ASCE Natl. Conv., 1984, p. 174–91.

[9] API. RP2A: Recommended practice for planning, designing and constructing offshore platforms - Working stress design. Washington, DC: 2007.

[10] Det Norske Veritas. DNV Offshore Standard DNV-OS-J101 Design of Offshore Wind Turbine Structures. 2011.

[11] Reese LC, Matlock H. Non-dimensional Solutions for Laterally Loaded Piles with Soil Modulus Assumed Proportional to Depth. Proc. 8th Int. Conf. Soil Mech. Found. Eng., Austin, TX: 1956, p. 1–41.

[12] Prendergast LJ, Hester D, Gavin K, O'Sullivan JJ. An investigation of the changes in the natural frequency of a pile affected by scour. J Sound Vib 2013;332:6685–702. doi:http://dx.doi.org/10.1016/j.jsv.2013.08.020i.

[13] Peder Hyldal Sørensen S, Bo Ibsen L. Assessment of foundation design for offshore monopiles unprotected against scour. Ocean Eng 2013;63:17–25. doi:10.1016/j.oceaneng.2013.01.016.

[14] Negro V, López-Gutiérrez J-S, Esteban MD, Matutano C. Uncertainties in the design of support structures and foundations for offshore wind turbines. Renew Energy 2014;63:125–32. doi:10.1016/j.renene.2013.08.041.

[15] Sumer BM, Fredsøe J, Christiansen N. Scour Around Vertical Pile in Waves. J Waterw Port, Coast Ocean Eng 1992;118:15–31.

[16] Klinga J V., Alipour A. Assessment of structural integrity of bridges under extreme scour conditions. Eng Struct 2015;82:55–71. doi:10.1016/j.engstruct.2014.07.021.

[17] Prendergast LJ, Hester D, Gavin K. Determining the presence of scour around bridge foundations using vehicle-induced vibrations. J Bridg Eng 2016;21. doi:10.1061/(ASCE)BE.1943-5592.0000931.

[18] Ju SH. Determination of scoured bridge natural frequencies with soil–structure interaction. Soil Dyn Earthq Eng 2013;55:247–54. doi:10.1016/j.soildyn.2013.09.015.

[19] Foti S, Sabia D. Influence of Foundation Scour on the Dynamic Response of an Existing Bridge. J Bridg Eng 2011;16:295–304. doi:10.1061/(ASCE)BE.1943-5592.0000146.

[20] Briaud JL, Hurlebaus S, Chang K, Yao C, Sharma H, Yu O, et al. Realtime monitoring of bridge scour using remote monitoring technology. vol. 7. Austin, TX: 2011.

[21] Elsaid A, Seracino R. Rapid assessment of foundation scour using the dynamic features of bridge superstructure. Constr Build Mater 2014;50:42–9. doi:10.1016/j.conbuildmat.2013.08.079.

[22] Prendergast LJ, Hester D, Gavin K. Development of a Vehicle-Bridge-Soil Dynamic Interaction Model for Scour Damage Modelling. Shock Vib 2016;2016.

[23] Prendergast LJ, Gavin K, Reale C. Sensitivity studies on scour detection using vibration-based systems. Transp Res Procedia 2016;14C:3982–9.

[24] May RWP, Ackers JC, Kirby AM. Manual on scour at bridges and other hydraulic structures. London: 2002.

[25] Sørensen SPH, Ibsen LB, Frigaard P. Experimental evaluation of backfill in scour holes around offshore monopiles. Proc. Second Int. Symp. Front. offshore Geotech., Perth, Western Australia: 2010, p. 617–22.

[26] Prendergast LJ, Gavin K, Doherty P. An investigation into the effect of scour on the natural frequency of an offshore wind turbine. Ocean Eng 2015;101:1–11. doi:10.1016/j.oceaneng.2015.04.017.

[27] Romano MC, Middendorp P, Doornbos S. Pile Foundation Design Philosophy and Testing Program for a New Generation Diesel Fuel Plant. Proc. Deep Found. Inst. (DFI)-Geotechnical Challenges Urban Regen., London, UK: 2010.

[28] Reale C, Xue J, Gavin K. Using reliability theory to assess the stability and prolong the design life of existing engineered slopes. Geotechnical Safety and Reliability, 2017, pp. 61-81

[29] Reale C, Xue J, Pan Z, Gavin K. Deterministic and probabilistic multi-modal analysis of slope stability. Comput Geotech 2015;66:172–9. doi:10.1016/j.compgeo.2015.01.017.

[30] Vanmarcke E. Probabilistic modeling of soil profiles. J Geotech Eng Div 1977;103:1227–46.

[31] Phoon K, Kulhawy F. Evaluation of geotechnical property variability. Can Geotech J 1999;36:625–39.

[32] Reale C, Xue J, Gavin K. System reliability of slopes using multimodal optimisation. Géotechnique 2016;66:413–23. doi:10.1680/jgeot.15.P.142.

[33] Baecher GB, Christian JT. Reliability and Statistics in Geotechnical Engineering. John Wiley & Sons; 2005.

[34] Cherubini C, Christian J. Factor of Safety and Reliability in Geotechnical Engineering. J Geotech Geoenvironmental Eng 2001;127:700–21. doi:http://dx.doi.org/10.1061/(ASCE)1090-0241(2001)127:8(700).

[35] Rackwitz R. Reviewing probabilistic soils modelling. Comput Geotech 2000;26:199–223. doi:10.1016/S0266-352X(99)00039-7.

[36] Low BK, Lacasse S, Nadim F. Slope reliability analysis accounting for spatial variation. Georisk Assess Manag Risk Eng Syst Geohazards 2007;1:177–89. doi:10.1080/17499510701772089.

[37] Doherty P, Gavin K. Statistical review of CPT data and implications for pile design. Proc. 2nd Int. Symp. Cone Penetration Test., 2010.

[38] Firouzianbandpey S, Griffiths D V., Ibsen LB, Andersen L V. Spatial correlation length of normalized cone data in sand : case study in the north of Denmark. Can Geotech J 2014;857:844–57. doi:10.1139/cgj-2013-0294.

[39] Jiang S-H, Li D-Q, Zhang L-M, Zhou C-B. Slope reliability analysis considering spatially variable shear strength parameters using a non-intrusive stochastic finite element method. Eng Geol 2014;168:120–8. doi:10.1016/j.enggeo.2013.11.006.

[40] Hicks MA, Samy K. Influence of heterogeneity on undrained clay slope stability. Q J Eng Geol Hydrogeol 2002;35:41–9. doi:10.1144/qjegh.35.1.41.

[41] Lloret-Cabot M, Fenton G, Hicks M. On the estimation of scale of fluctuation in geostatistics. Georisk Assess Manag Risk Eng Syst Geohazards 2014;8:129–40. doi:10.1080/17499518.2013.871189.

[42] Fenton G. Random field modeling of CPT data. J Geotech Geoenvironmental Eng 1999;125:486–98. doi:http://dx.doi.org/10.1061/(ASCE)1090-0241(1999)125:6(486).

[43] Hicks M, Jommi C. Stochastic Analysis and Inverse Modelling. ALERT Geomaterials; 2014.

[44] Kasama K, Whittle AJ. Effect of spatial variability on the slope stability using Random Field Numerical Limit Analyses. Georisk Assess Manag Risk Eng Syst Geohazards 2015;10:42–54. doi:10.1080/17499518.2015.1077973.

[45] Fenton GA, Griffiths D V. Bearing-capacity prediction of spatially random c – ϕ soils. Can Geotech J 2003;40:54–65. doi:10.1139/t02-086.

[46] Fenton G, Griffiths D. Probabilistic foundation settlement on spatially random soil. J Geotech Geoenvironmental Eng 2002;128:381–90.

[47] Kwon YW, Bang H. The Finite Element Method using MATLAB. Boca Raton, FL: CRC Press, Inc.; 2000.

[48] Dong RG. Effective mass and damping of submerged structures. 1978.

[49] Corciulo S, Zanoli O, Pisano F. Transient response of offshore wind turbines on monopiles in sand: role of cyclic hydro-mechanical soil behaviour. Comput Geotech 2017;83:221–38. doi:10.1016/j.compgeo.2016.11.010.

[50] Siemens Wind Power. Wind Turbine SWT-3.6-120 Technical Specifications. Hamburg: 2009.

[51] Winkler E. Theory of elasticity and strength. Dominicus Prague: 1867.

[52] Dutta SC, Roy R. A critical review on idealization and modeling for interaction among soil–foundation–structure system. Comput Struct 2002;80:1579–94. doi:10.1016/S0045-7949(02)00115-3.

[53] Prendergast LJ, Gavin K. A comparison of initial stiffness formulations for small-strain soil – pile dynamic Winkler modelling. Soil Dyn Earthq Eng 2016;81:27–41. doi:10.1016/j.soildyn.2015.11.006.

[54] Versteijlen WG, Metrikine a. V., van Dalen KN. A method for identification of an effective Winkler foundation for large-diameter offshore wind turbine support structures based on in-situ measured small-strain soil response and 3D modelling. Eng Struct 2016;124:221–36. doi:10.1016/j.engstruct.2016.06.007.

[55] Pierson W, Moskowitz L. A proposed spectral form for fully developed wind seas based on the similarity theory of SA Kitaigorodskii. J Geophys Res 1964;69.

[56] Hsu SA, Meindl EA, Gilhousen DB. Determining the power-law wind-profile exponent under near-neutral stability conditions at sea. J Appl Meteorol 1994;33:757–65.

[57] Morison J, Johnson J, Schaaf S. The force exerted by surface waves on piles. J Pet Technol 1950;2.

[58] Corciulo S. Dynamic Hydro-Mechanical Analysis of Soil-Monopile Interaction in Offshore Wind Turbines. Politecnico Di Milano, 2015.

[59] Fenton J, McKee W. On calculating the lengths of water waves. Coast Eng 1990;14:499–513.

[60] Donohue S, Long M, Gavin K, O'Connor P. Shear Wave Stiffness of Irish Glacial Till. Int. Conf. Site Characterisation I, Porto, Portugal: 2004, p. 459–66.

[61] Lunne T, Robertson PK, Powell JJM. Cone Penetration Testing in Geotechnical Practice. Blackie Academic and Professional; 1997.

[62] Schnaid F, Lehane BM, Fahey M. In situ test characterisation of unusual geomaterials. Proc. Int. Conf. Site Characterisation, Porto, Portugal: 2004, p. 49–73.

[63] Ashford SA, Juirnarongrit T. Evaluation of Pile Diameter Effect on Initial Modulus of Subgrade Reaction. Geotech Geoenvironmental Eng 2003;129:234–42. doi:10.1061/(ASCE)1090-0241(2003)129:3(234).

[64] Vesic AB. Bending of beams resting on isotropic elastic solid. J Soil Mech Found Eng 1961;87:35–53.

[65] Tempel J Van Der, Molenaar D. Wind Turbine Structural Dynamics – A Review of the Principles for Modern Power Generation , Onshore and Offshore. Wind Eng 2002;26:211–20.

[66] API. API RP2A-WSD. 2007.

[67] Suryasentana SK, Lehane BM. Numerical derivation of CPT-based p – y curves for piles in sand. Geotechnique 2013.

[68] Kulhawy FH, Mayne PW. Manual on estimating soil properties for foundation design No. EPRI-EL-6800. Ithaca, NY (USA): 1990.

[69] Kallehave D, Thilsted CL, Liingaard MA. Modification of the API P-Y Formulation of Initial Stiffness of Sand. Proc. 7th Int. Conf. Offshore Site Investig. Geotech., London, UK: 2012, p. 465–72.

[70] Det Norske Veritas. DNV Offshore Standard DNV-OS-J101 Design of Offshore Wind Turbine Structures. 2007.